REVIEW

Check for
updates

Effect of Tube-to-Pellet Diameter Ratio on Turbulent Hydrodynamics in Packed Beds: A Magnetic Resonance Velocity Imaging Study

Scott V. Elgersma[1] · Andrew J. Sederman[1] · Michael D. Mantle[1] ·
Constant M. Guédon[2] · Gary J. Wells[3] · Lynn F. Gladden[1]

Abstract

The hydrodynamics in packed reactors strongly influences reactor performance. However, limited experimental techniques are capable of non-invasively measuring the velocity field in optically opaque packed beds at the turbulent flow conditions of commercial relevance. Here, compressed sensing magnetic resonance velocity imaging has been applied to investigate the hydrodynamics of turbulent flow through narrow packed beds of hollow cylindrical catalyst support pellets as a function of the tube-to-pellet diameter ratio, N, for $N = 2.3$, 3.7, and 4.8. 3D images of time-averaged velocity for the gas flow through the beds were acquired at constant Reynolds number, $Re_p = 2500$, at a spatial resolution of 0.70 mm (x) $\times$ 0.70 mm (y) $\times$ 1.0 mm (z). The resulting flow images give insight into the bed and pellet scale hydrodynamics, which were systematically compared as a function of N. Some changes in hydrodynamics with N were observed. Namely, the near-wall hydrodynamics changed with N, with the $N = 4.8$ bed showing higher velocity at the wall compared to the $N = 2.3$ and $N = 3.7$ beds. Further, in the $N = 3.7$ bed, channels of high velocity, termed flow lanes, were found 1.3 particle diameters from the wall, possibly due to the bed structure in this particular bed. At the pellet scale, the hydrodynamics were found to be independent of N. The results reported here demonstrate the capability of magnetic resonance velocity imaging for studying turbulent flows in packed beds, and they provide fundamental insight into the effect of N on the hydrodynamics.

Extended author information available on the last page of the article

1 Introduction

Packed bed reactors are extensively used in the chemical industry to facilitate various heterogeneously catalysed processes, including steam methane reforming, oxidative coupling of methane, epoxidation of ethylene, hydrogenation, and hydrodesulfurization of crude oils, hydrodeoxygenation of biofuels, and the Fischer–Tropsch (FT) process, among others [1–3]. A common type of packed bed reactor consists of a tubular vessel loaded with catalyst pellets, through which fluid reactants are passed where they react at the catalyst surface to form a desired product. The hydrodynamics and heat transfer in packed beds are important, especially for highly exothermic processes to avoid the formation of local 'hot spots' in the reactor which often have a detrimental effect on reactor selectivity.

The tube-to-pellet diameter ratio, $N = d_{tube}/d_o$, where d_{tube} is the tube diameter and d_o is the outer diameter of the catalyst pellet, is well known to impact both the bed structure [4–6] and heat transfer properties [7–9] within packed bed reactors. Due to enhanced wall-to-bed heat transfer compared to large beds, narrow packed beds (commonly defined as ~ 2–$3 \leq N \leq 10$ [10]), are used in processes where good heat transfer is essential, for example highly exothermic reactions such as syngas production (e.g. dry reforming and steam reforming of methane) and ethylene epoxidation. For spherical pellets at very low tube-to-pellet diameter ratios, $N \leq 4$, reported measurements of average voidage [11] and heat transfer [8] (both thermal conductivity and wall heat transfer coefficient) show a large degree of scatter and do not appear to trend with any simple correlation. Recently this issue has been the subject of considerable attention in the literature. Guo et al. [12] have shown that the radial voidage profile for beds of spheres with $N \leq 3.4$ can show anomalous results depending on the exact value of N, with a peak in the voidage profile at the centre of the bed in some cases. Dixon [13] recently demonstrated that the complex relationship between radial heat transfer and N is largely due to substantial changes in the bed structure depending on the particular value of N over the range of $2 < N < 4$. It follows that because small changes in N can lead to large changes in local bed structure, and thus flow and transport properties, standard correlations for narrow beds ($N < 4$) may give considerable error for any particular value of N [13, 14]. Particle-resolved computational fluid dynamics (CFD) may offer a path forward for accounting for the ordering effects observed in small N beds. However, obtaining an accurate simulation of the bed structure for real catalyst pellets used in packed bed reactors can be difficult since pellet material, friction, and loading method can all affect the final bed structure [15, 16].

Accurately predicting the structure and transport properties in narrow beds is difficult, even for model spherical pellets. Detailed, pellet scale, measurements of the velocity field within narrow packed beds may help fundamentally understand how changes in bed structure with N impact the hydrodynamics, and ultimately the transport properties. Whilst numerous studies have investigated the bed structure and heat transport, few have focused on the velocity field in narrow packed beds as a function of N. Bey and Eigenberger [17, 18] measured the average radial velocity profile at the outlet of packed beds over a range of N using

hot-wire anemometry, observing changes in the velocity profile that corresponded to changes in the voidage profile. However, these hot-wire anemometry measurements only probe the hydrodynamics at the bed exit and do not indicate if the flow field within the bed changes as a function of N at either the bed or pellet scale. In contrast, using magnetic resonance (MR) velocity imaging, it is possible to obtain quantitative measurements of bed structure and flow at the pellet scale in packed beds. Blümich and co-workers [19–21] used 2D MR velocity imaging to investigate the hydrodynamics at both the bed and pellet scale for laminar liquid flow (pellet Reynolds number $Re_p \leq 300$) in packed beds over a range of $N = 1.4$–32. They observed the radial velocity profile to follow a strong oscillatory trend consistent with the ordering of the pellets in narrow packed beds, with the highest fluid velocity observed near the tube wall for all beds except at $N = 32$ and $N = 2.7$. The result at $N = 2.7$ is especially interesting, as the flow was observed to be fastest at the centre of the bed due to a large void at the centre the bed for this particular value of N [21], thereby demonstrating the strong correlation between wall ordering, bed structure, and hydrodynamics in narrow packed beds. Commercial packed bed reactors typically operate in the turbulent flow regime ($Re_p \geq 500$), and, therefore, the effect of N on the hydrodynamics in packed beds in the turbulent regime is of significant interest. Using MR velocity imaging, it is possible to acquire quantitative images of the time-averaged velocity for turbulent flows in packed beds and similar systems. Cooper et al. [22, 23] used spin echo single point imaging (SESPI) to obtain time-averaged velocity images of turbulent flow through a structured monolith (channel Reynolds number $Re_c = 200$–1100). Recently, Elgersma et al. [24] applied the SESPI pulse sequence to acquire 3D images of the time-averaged velocity and turbulent kinetic energy for turbulent flow through beds of α-alumina catalyst pellets over a range of turbulent flow conditions ($Re_p = 500$–6500) in a narrow packed bed ($N = 4.7$).

To date, no systematic comparison of the pellet-scale velocity field within packed beds as a function of N has been reported for the turbulent flow conditions of commercial interest. The aim of this work is to apply compressed sensing MR velocity imaging to investigate the velocity field as a function of N in beds of commercially relevant pellets at turbulent flow conditions. From these data, it is possible to assess the degree to which the flow field depends on N at both the bed and pellet scale, and to further understand the coupling between bed structure and transport properties in narrow packed beds. This paper is structured as follows. First, details of the rig and magnetic resonance techniques used for imaging the turbulent flow in narrow packed beds are reported. The time-averaged velocity field has been measured in 3D, using compressed sensing MR velocity imaging, for flow through beds of varying diameter packed with hollow cylindrical pellets with N ranging from $N = 2.3$–4.8. The range of N studied herein, whilst limited due to size constraints of both the catalyst pellets and the radio frequency probe, enables the investigation of the hydrodynamics as a function of N in very narrow beds typical of those used commercially for very exothermic reactions. The flow at both the bed and pellet scale is investigated as a function of N. The results are discussed in the context of previously reported observations of structure and flow in narrow packed beds. These measurements give valuable experimental insight into the effect that the tube-to-pellet diameter ratio has

on flow in a system of commercially relevant pellets at the turbulent flow conditions of true commercial interest.

2 Materials and Methods

2.1 Materials, Equipment, and Experimental Conditions

Three beds with different tube-to-pellet diameter ratios, N, were investigated in this work using acrylonitrile butadiene styrene (ABS) plastic pipes of diameter, d_{tube}, of 20, 32, and 41 mm (ID), packed with porous hollow cylindrical α-alumina catalyst support pellets (Shell Global Solutions, Amsterdam), details of which are given in Table 1. The spherical equivalent particle diameter, $d_{\text{e}} = 6V_{\text{p}}/A_{\text{p}}$ (e.g. the sphere with the same surface area to volume ratio as the pellet), is also given in Table 1. The pellet volume, $V_{\text{p}} = \frac{\pi}{4}L\left(d_{\text{o}}^2 - d_{\text{hole}}^2\right)$, and external surface area, $A_{\text{p}} = \pi L\left(d_{\text{o}} + d_{\text{hole}}\right) + \frac{\pi}{2}\left(d_{\text{o}}^2 - d_{\text{hole}}^2\right)$, were calculated based on the average pellet shape without considering surface roughness. The resulting tube to particle diameter ratio, $N = d_{\text{tube}}/d_{\text{o}}$, used in this study ranged from $N = 2.3$–4.8.

Sulphur hexafluoride (SF_6) was utilized as the nuclear magnetic resonance (NMR)-active gas in this study, due to its high density, high gyromagnetic ratio, and favourable NMR relaxation properties (short T_1), as discussed by Sankey et al. [25] and Ramskill et al. [26]. The closed-loop recirculating flow rig utilized by Elgersma et al. [24], which is depicted in Fig. 1, was used for packed bed flow experiments. Plastic perforated plate distributors fixed at the inlet and outlet provided even flow distribution to the packed bed. The flow was imaged approximately 1 m downstream of the entrance, thereby ensuring fully developed flow in the imaging region.

Details of the packed beds and process conditions used are reported in Table 2. All experiments were conducted at a nominal pellet Reynolds number of $Re_{\text{p}} = 2500$, where $Re_{\text{p}} = \frac{\rho d_{\text{e}} U_{\text{int}}}{\mu}$ where ρ is the gas density, μ is the gas viscosity, ϵ is the bed voidage and $U_{\text{int}} = U_0/\epsilon$ is the average interstitial velocity in the bed computed by dividing the superficial (open-tube) velocity, U_0, by the bed voidage, ϵ. The bed voidage was determined gravimetrically by measuring the mass of catalyst loaded into the bed (of known volume). The density of SF_6 at the process conditions used was taken from Guder & Wagner [27] and the viscosity at the process conditions used was taken as 1.5×10^{-5} Pa s [28]. For the $N = 2.3$ bed, because of the limited number of pellets in the imaging region, imaging experiments were conducted for

Table 1 Average pellet properties

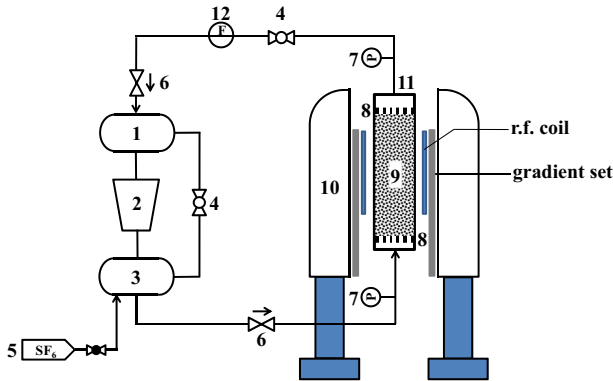| Pellet shape	Cylinder with hole
Material	α-Alumina
Pellet length, L (mm)	8.7
Hole diameter, d_{hole} (mm)	1.3
Outer diameter, d_{o} (mm)	8.6
Spherical equivalent diameter, d_{e} (mm)	7.7

Fig. 1 Schematic diagram of the recirculating SF_6 flow rig used for MR velocity imaging in packed beds. *1* low-pressure vessel; *2* compressor; *3* high-pressure vessel; *4* needle valve; *5* SF_6 gas cylinder; *6* regulator valve; *7* digital pressure gauge; *8* perforated plate distributor; *9* catalyst support pellets; *10* superconducting magnet, 4.7 T; *11* ABS pipe (various diameters used); *12* mass flow controller (Bronkhorst model F-113AC-M50-AAD-55-E)

Table 2 Details of the packed beds and process conditions used for MR velocity imaging experiments

$N = \frac{d_{tube}}{d_o}$ (–)	4.8	3.7	2.3
d_{tube} (mm)	41	32	20
P [bar(a)]	7.6	7.2	6.9
$\dot{m}$ (g min^{-1})	158	106	48
ρ (kg m^3)	49.6	46.7	43.8
U_0 (m s^{-1})	0.040	0.047	0.057
ϵ, gravimetric (–)	0.41 ± 0.02	0.45 ± 0.02	0.52 ± 0.02
Re_p (–)	2497	2506	2514
Re_p, nominal (–)	2500	2500	2500

Note that pressure is given as absolute pressure

two separate sections of the bed to ensure that the flow data were more representative of the entire bed and not merely the local bed structure. The two different positions of the $N = 2.3$ bed that were imaged are herein referred to as pos. (position) A and pos. B.

2.2 Magnetic Resonance Experiments

All experiments were conducted using a 4.7 T vertical bore superconducting magnet (Bruker Spectrospin DMX200), equipped with a 64 mm birdcage r.f. coil tuned to a ^{19}F resonant frequency of 187.64 MHz. A triaxial gradient set was used (Bruker Mini 0.36), with a maximum gradient strength of 13.1 G cm^{-1} in all three orthogonal directions.
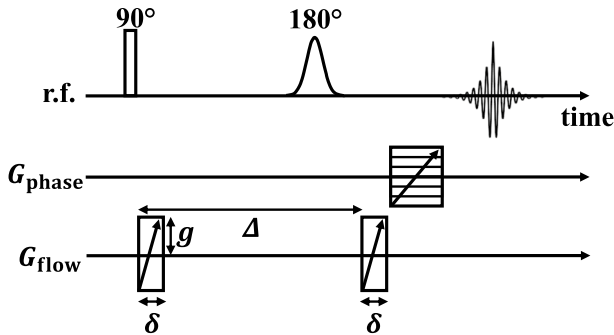
Fig. 2 SESPI pulse sequence used for MR velocity imaging

The SESPI pulse sequence, shown in Fig. 2, was used for all imaging experiments conducted in this work [29, 30]. This pure phase-encode sequence was selected as it has been previously utilized for acquiring quantitative velocity images in highly turbulent systems [23, 24]. Similar imaging parameters to that reported by Elgersma et al. [24] were used in this work and are summarized below. The SESPI sequence was used to acquire 3D images of both the bed structure, and the time-averaged velocity, $\bar{\mathbf{u}}$. For imaging of the bed structure, and the time-averaged velocity, only the magnitude and direction of the flow encoding gradient, g, was varied. All other imaging parameters were maintained constant and are described here. For the $d_{tube} = 32$ mm and $d_{tube} = 41$ mm tubes, images were acquired with a field of view (FOV) of 45 mm (x) × 45 mm (y) × 64 mm (z) on a 64 × 64 × 64 matrix resulting in images with a resolution of 0.70 mm (x) × 0.70 mm (y) × 1.0 mm (z). For the $d_{tube} = 21$ mm tube the FOV was reduced to 22.5 mm (x) × 22.5 mm (y) × 64 mm (z) and thus a 32 (x) × 32 (y) × 64 (z) image raster was used to achieve the same resolution as used for the larger tubes. Spatial resolution was achieved by independently incrementing the position encoding gradient (G_{phase} in Fig. 2) in the three orthogonal directions. The duration of G_{phase} was 0.2 ms, with a gradient stabilization delay of 0.2 ms and a ramp time of 0.02 ms. For signal excitation, a hard 90° r.f. pulse of duration 92 μs was used. A Gaussian shaped 180° soft pulse of duration 512 μs was used for spin-echo refocusing and to act as an effective bandwidth filter (and avoid spurious background signals). The echo time was 2.47 ms, and the recycle time was 100 ms (note that the recycle time was much longer than $T_1 \approx T_2 \approx 15$ ms due to gradient cooling limitations). Signal was acquired at a sweep width of 100 kHz. To increase the signal to noise ratio (SNR), 8 complex points from each free induction decay were averaged together (adding more was found to result in significant T_2^* weighting). Four scans were collected to complete a full phase cycle of the SESPI pulse sequence.

To image the bed structure, the flow encoding gradient was turned off, $g = 0$, and the SESPI experiment was conducted with 7 bar(a) of SF_6 in the bed and no flow. For imaging of the three orthogonal components of time-averaged velocity, $\bar{u}_x, \bar{u}_y, \bar{u}_z$, flow encoding was achieved using gradient pulses (depicted as G_{flow} in Fig. 2) of duration $\delta = 0.48$ ms on either side of the 180° r.f. refocusing pulse, and a flow encoding

duration of $\Delta = 1.69$ ms. The gradient pulse magnitude, g, was set empirically to avoid phase aliasing, with typical gradient strengths ranging from $g = 0.2$–2 G cm^{-1}. Two images were acquired at equal, but opposite, gradient strengths $(+g, -g)$ and the phase difference between the two images, ϕ, was taken and used to compute the time-averaged velocity using the well-known relation [31]:

$$\phi = \gamma \Delta \delta g \overline{u}_i, \tag{1}$$

where γ is the gyromagnetic ratio of the ^{19}F nucleus and $\overline{u}_i$ is the time-averaged velocity in the direction of the applied gradients (denoted i). Each velocity image was corrected for phase shifts caused by gradient eddy currents by acquiring an image at zero-flow conditions and subtracting the zero-flow phase map from the phase map acquired at flowing conditions.

The uncertainty in the time-averaged velocity maps, computed from the SNR of the acquired images [32], was $< 0.2\ \overline{u}_i/U_{int}$. To confirm the quantitative nature of the velocity images, the flow rate at each axial position in the bed was calculated from the 3D images of time-averaged velocity in the axial direction, $\overline{u}_z$. In all cases the flow rate calculated from the MR results agreed within $\leq 6.2\%$ discrepancy with the known flow rate (set using a mass flow controller) over a 45 mm central section of the imaging FOV (in the z-direction). This central 45 mm region was subsequently used for all visualization and analysis reported in this work, providing a region of the bed approximately 5 pellet layers high.

2.3 Compressed Sensing and Image Reconstruction

Due to the slow nature of the pure phase-encode SESPI sequence used, compressed sensing (CS) [33] was implemented to accelerate data acquisition. The approach to implement CS in this work, namely the sampling scheme design and reconstruction, is identical to that utilized in Elgersma et al. [24], and is summarized here. A bespoke sampling scheme was generated for each bed from a 3D image of the bed structure (i.e. a ^{19}F spin density image) using the method of Karlsons et al. [34]. The 3D bed structural images were obtained by fully sampling **k**-space for each bed, with acquisition times of 29 h for the $d_{tube} = 32$ mm and $d_{tube} = 41$ mm tubes, and 7 h for the $d_{tube} = 20$ mm tube (due to the smaller raster size). Based on the optimization conducted by Elgersma et al. [24] a sampling fraction of 16% was used for generating a 3D sampling pattern for each bed, with undersampling in all three dimensions of **k**-space. The sampling patterns were then used for all MR velocity image acquisitions. Total variation (TV) regularization was used to reconstruct the undersampled images, due to its good edge preservation [23, 26]:

$$\mathbf{x} \in \text{argmin}_{\mathbf{x}} \left\{ \frac{1}{2} \|\mathbf{y} - W\mathcal{F}\mathbf{x}\|_2^2 + \alpha \|\nabla \mathbf{x}\|_2 \right\}, \tag{2}$$

where $\mathbf{y}$ is the acquired (undersampled) MR signal in **k**-space, W is the sampling pattern, $\mathcal{F}$ is the Fourier transform operator, α is the regularization parameter, and $\mathbf{x}$ is the reconstructed image. Equation (2) was solved using the object oriented mathematics for inverse problems (OOMFIP) toolbox developed by Benning and

co-workers [35], using a regularization parameter of $\alpha = 0.1$ and 8 Bregman iterations, selected based on the optimization conducted by Elgersma et al. [24]. By only sampling 16% of **k**-space, the usage of CS reduced data acquisition times by a factor of 6.3. Thus, with compressed sensing, acquiring a 3D image of one component of the time-averaged velocity took 9.2 h for the 41 mm and 32 mm diameter tubes and 2.3 h for the 20 mm diameter tube.

For all image visualization and spatial analysis conducted herein, the **k**-space data associated with the reconstructed velocity images were zero-filled from $64 \times 64 \times 64$ to $128 \times 128 \times 128$ for the 41 mm and 32 mm diameter tubes, and $32 \times 32 \times 64$ to $64 \times 64 \times 128$ for the 20 mm diameter tube to increase the available spatial resolution. Image reconstruction and analysis were conducted using Matlab 2021 (Mathworks), and 3D image rendering and individual pellet segmentation were conducted using Amira-Avizo 2021.1 (ThermoFisher Scientific).

3 Results and Discussion

3.1 Time-Averaged Velocity Images and Bed Scale Hydrodynamics

2D images, extracted from the 3D image of the time-averaged axial velocity in each bed, $\overline{u}_z$, normalized by the mean interstitial velocity, U_{int}, are shown in Figs. 3 and 4. Qualitatively, the velocity images show a similar level of flow heterogeneity irrespective of N, with regions of fast flow located in large voids, between pellets, and near the walls whilst regions of low velocity are located in the pellet wakes and in the holes of some pellets. Some flow 'lanes' are observed in the velocity image shown in Fig. 3b for the $N = 3.7$ bed where a channel of high axial velocity is seen approximately one pellet diameter from the wall along the length of the image. Whilst this may be an effect of the highly structured nature of this narrow bed, it is important to not over-interpret this as only a 2D slice through the complex
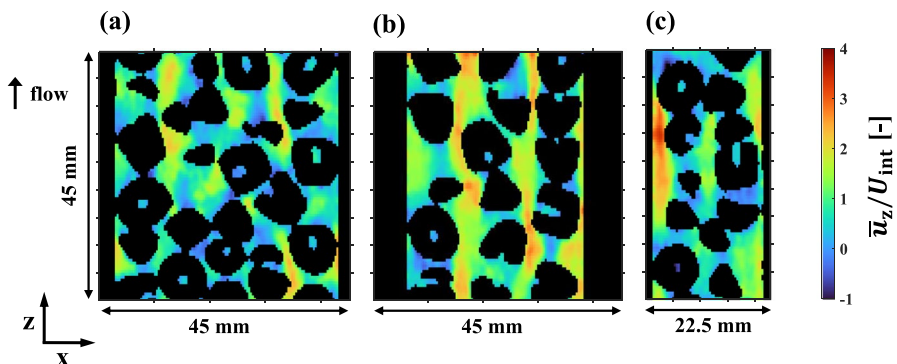

Fig. 3 Central transverse slice of 3D image of time-averaged axial velocity in each bed at $Re_p = 2500$: **a** $N = 4.8$; **b** $N = 3.7$; **c** $N = 2.3$. Images shown in **a** and **b** have a FOV of 45 mm (x) × 45 mm (z) while the image shown in **c** has an FOV of 22.5 mm (x) × 45 mm (z). All images have an in-plane spatial resolution of 0.35 mm (x) × 0.5 mm (z)
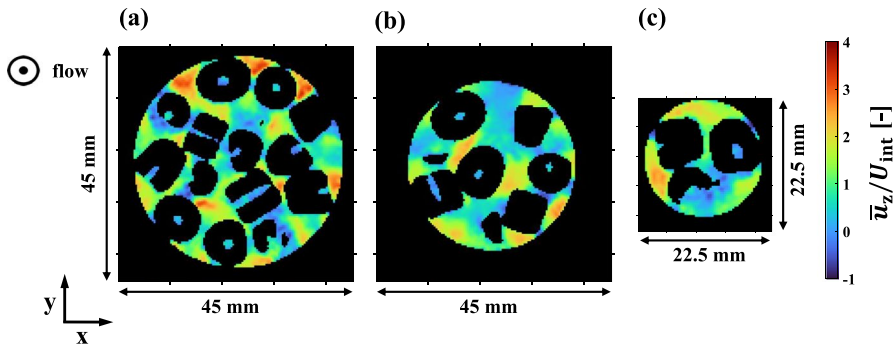
Fig. 4 Central axial slice of 3D image of time-averaged axial velocity in each bed at $Re_p = 2500$: **a** $N = 4.8$; **b** $N = 3.7$; **c** $N = 2.3$. Images shown in **a** and **b** have a FOV of 45 mm (x) × 45 mm (y) while the image shown in **c** has an FOV of 22.5 mm (x) × 22.5 mm (y). All images have an in-plane spatial resolution of 0.35 mm (x) × 0.35 mm (y)

3-dimensional flow field is shown. The potential effect of flow channelling and flow 'lanes' can be better investigated with the radial profile of velocity, as discussed later Sect. 3.2.

To investigate the velocity field at the bed scale, Fig. 5 shows the distribution of normalized axial velocity, $\overline{u}_z/U_{int}$, normalized transverse (y-direction) velocity, $\overline{u}_y/U_{int}$, and normalized velocity magnitude, $|\overline{u}|/U_{int}$, for each bed. Considering the variability between the measurements for the $N = 2.3$ bed at two different positions, the distributions for the axial velocity, transverse velocity, and velocity magnitude all appear similar as a function of N. The one exception to this similarity is the high-velocity tail in the axial velocity and velocity magnitude distribution. The $N = 4.8$ bed shows a marginally larger tail for high axial velocities
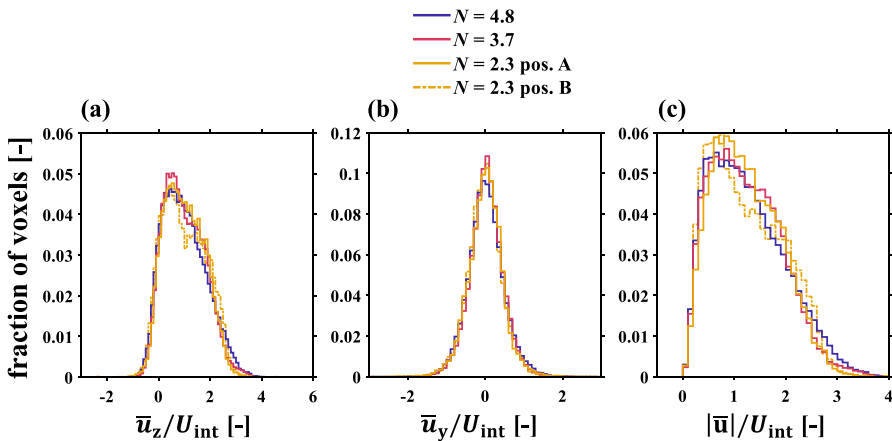
Fig. 5 Histograms of **a** time-averaged normalized axial velocity, $\overline{u}_z/U_{int}$, **b** time-averaged normalized transverse (y) velocity, $\overline{u}_y/U_{int}$, and **c** time-averaged normalized velocity magnitude, $|\overline{u}|/U_{int}$
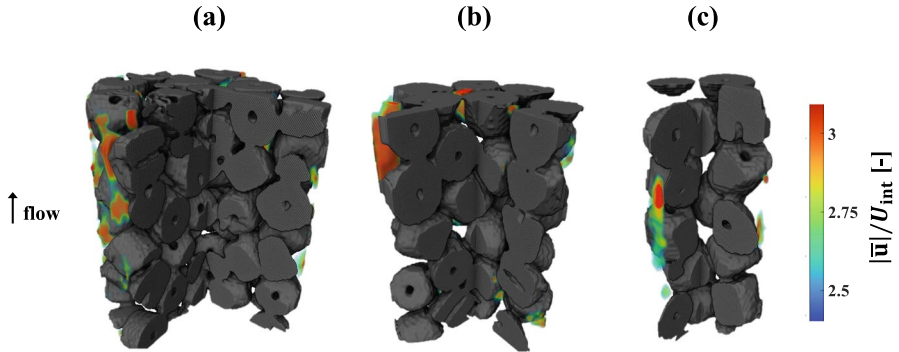
Fig. 6 3D visualization of regions of the bed with high-speed fluid, $|\overline{\mathbf{u}}|/U_{int} > 2.5$ at $Re_p = 2500$ for **a** $N = 4.8$; **b** $N = 3.7$; **c** $N = 2.3$ (Pos. A)

Table 3 Fraction of fluid, f, with zero or negative velocity in the axial direction (backflow), $\overline{u}_z/U_{int} \leq 0$, and high-speed fluid, $|\overline{\mathbf{u}}|/U_{int} > 2.5$, in each bed at $Re_p = 2500$

N	$f(\overline{u}_z/U_{int} \leq 0)$	$f(|\overline{\mathbf{u}}|/U_{int} > 2.5)$
4.8	0.102	0.064
3.7	0.083	0.040
2.3 pos. A	0.084	0.032
2.3 pos. B	0.111	0.044

The average uncertainty in the metrics, estimated by splitting each bed into two domains and taking the discrepancy between the backflow/high-speed fluid fraction calculated for each domain, is ~ ± 0.004, ± 0.01, and ± 0.02 for the $N = 4.8$, $N = 3.7$, and $N = 2.3$ beds, respectively

($\overline{u}_z/U_{int} > \sim 2.5$) and high-velocity magnitudes ($|\overline{\mathbf{u}}|/U_{int} > \sim 2.5$) compared to the smaller N beds. This marginally larger tail in the velocity distribution may be due to increased structural heterogeneity in the $N = 4.8$ bed compared to the lower N beds where wall structuring effects become increasingly important. Magnico [36] compared the velocity distributions for laminar flow in beds of spheres with different N using CFD. Interestingly, the distributions predicted by CFD showed little change with N, in general agreement with the results reported here, with the exception of the high-velocity tail in the $N = 4.8$ bed.

Regions of the bed with high-speed fluid, $|\overline{\mathbf{u}}|/U_{int} > 2.5$, are shown in Fig. 6. The high-speed fluid is seen to be predominantly in pockets near the wall, with very little high-speed fluid in the core of the bed. The corresponding fraction of high-speed fluid, as well as the fraction of backflow ($\overline{u}_z/U_{int}$) are reported in Table 3. These fractions were computed by appropriately integrating the velocity histograms shown in Fig. 5. The backflow fraction is approximately constant with respect to N, which is also reflected by the velocity distribution shown in Fig. 5a. There is marginally more high-speed fluid in the $N = 4.8$ bed compared to the smaller N beds, which again is reflected in Fig. 5c. Taken together, the velocity field measurements reported here indicate that the turbulent flow at the bed-scale

in this system is relatively independent of the tube-to-pellet diameter ratio N, with the exception of high-speed fluid in the bed. The slightly larger amount of high-speed fluid observed in the $N = 4.8$ bed is predominantly located near the tube wall, indicating that the velocity distribution in the narrower beds ($N = 3.7$, 2.3) is somewhat closer to uniform in nature.

3.2 Radial Profiles of Axial Velocity and Near-Wall Hydrodynamics

The radial profiles of voidage and axial velocity in each bed are shown in Fig. 7. In each bed, the voidage and velocity profiles show radial oscillations, which are well-known to occur in narrow packed beds due to pellet ordering at the wall [17, 19, 20, 37]. The radial profile of axial velocity shows a strong positive correlation with the radial voidage profile (with correlation coefficient, $\rho_c = 0.84$–0.85 for all the beds studied here), demonstrating the link between bed structure and flow in each of these beds. Each bed shows a similar degree of flow heterogeneity, reflected by the width
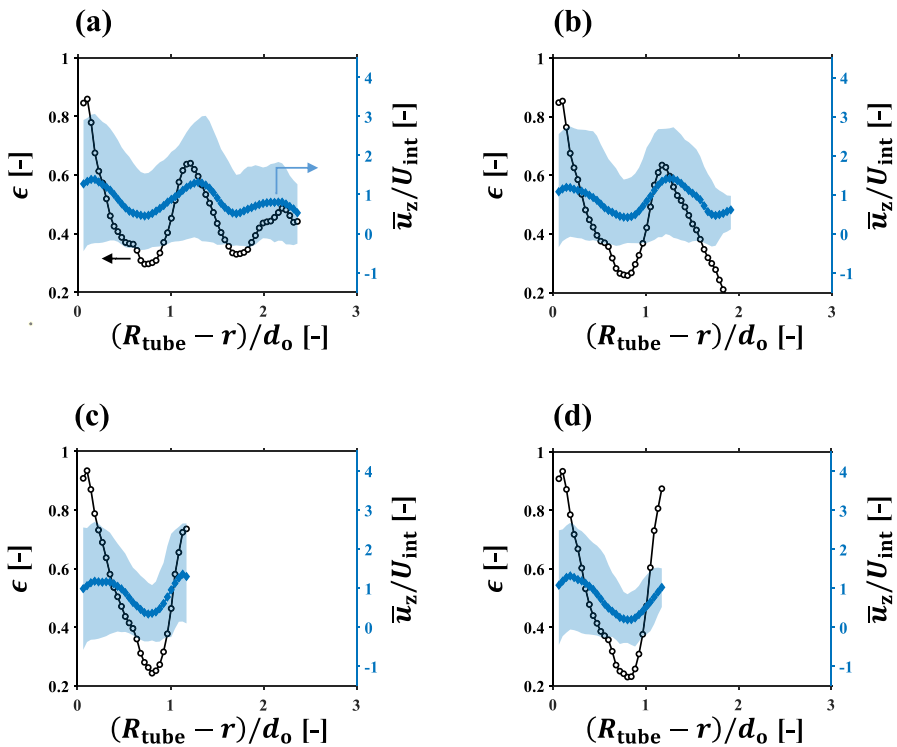
Fig. 7 Radial profile of voidage, $\epsilon(r)$, and normalized time-averaged axial velocity, $\bar{u}_z(r)/U_{int}$, as a function of distance from the tube wall, $R_{tube} - r$, normalized by pellet outer diameter, d_o. **a** $N = 4.8$ bed; **b** $N = 3.7$ bed; **c** $N = 2.3$ bed pos. A; **d** $N = 2.3$ bed pos. B. Shaded regions represent 2.5 percentile to 97.5 percentile of velocity values found at each respective radial position in the 3D flow images
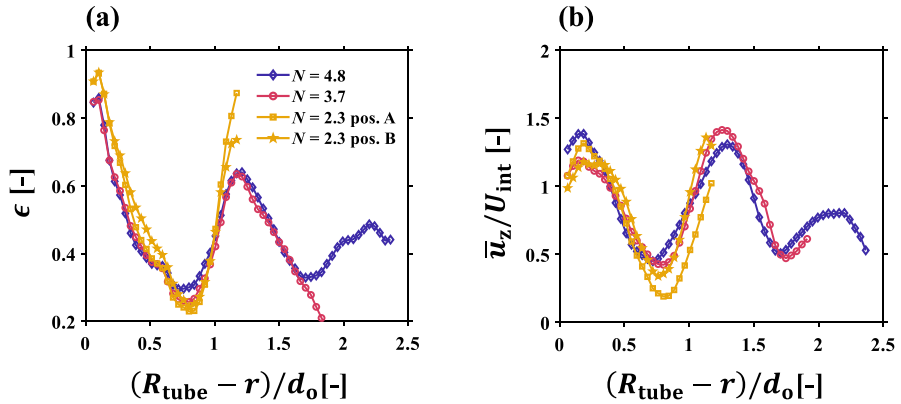
Fig. 8 Radial profile of **a** voidage, $\epsilon(r)$, and **b** normalized time-averaged axial velocity, $\bar{u}_z/U_{int}$, in each bed
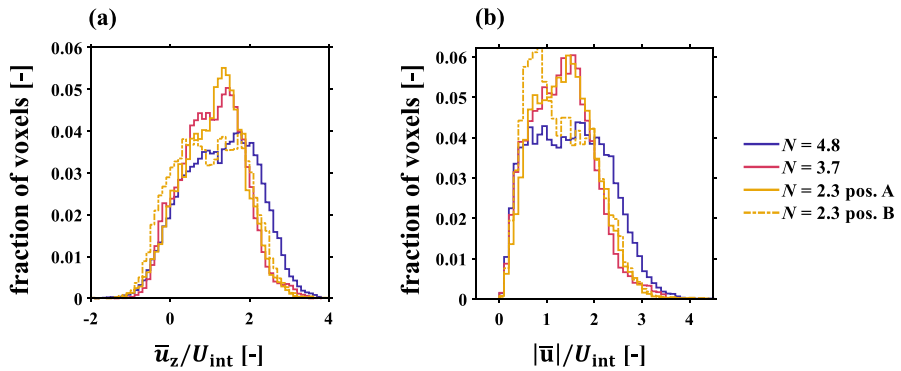

Fig. 9 Distribution of axial velocity and velocity magnitude for voxels adjacent to the tube wall (0.35 mm from tube wall) in each bed. **a** Time-averaged normalized axial velocity, $\bar{u}_z/U_{int}$; **b** time-averaged velocity magnitude, $|\bar{\mathbf{u}}|/U_{int}$

of the shaded velocity band in Fig. 7 showing the 2.5 percentile to 97.5 percentile velocity values at each radial position. Backflow ($\bar{u}_z/U_{int} \le 0$) is observed to occur throughout the bed, independent of radial position. The fluid with the largest axial velocity in the bed is found close to the tube wall and at radial positions where there is a local maxima in the voidage profile.

To facilitate comparison of the radial profiles as a function of N, the average radial profile of axial velocity and voidage for each bed are plotted together in Fig. 8. The voidage profiles show similar shapes for the beds across different N, however, some small differences can be observed, with the $N = 2.3$ bed showing higher void-age for distances $< 0.5\, d_o$ from the wall, compared to the larger beds. Further, the $N = 2.3$ and $N = 3.7$ beds show a slightly lower first minimum in the voidage profile compared to the $N = 4.8$ bed. The resulting radial profiles of average axial velocity trend well together for all N, except near the wall where the average axial velocity is

found to be larger near the wall in the $N = 4.8$ bed compared to the smaller beds. To further investigate this difference in the near-wall flow behaviour, Fig. 9 shows the distribution of time-averaged axial velocity and time-averaged velocity magnitude for voxels adjacent to the tube wall. The $N = 4.8$ bed shows a distinctively larger high-velocity tail compared to the smaller beds, thus resulting in a higher average velocity at the wall (as seen in Fig. 9). Interestingly, for the $N = 3.7$ bed, the average axial velocity at a distance $\sim 1.3\ d_o$ from the wall is larger than the velocity immediately adjacent to the wall (as seen in Fig. 8b). This observation helps to confirm that the flow lanes observed in the velocity images in Fig. 3b are somewhat representative of the 3D flow field in the bed.

The radial voidage profile in beds of spherical pellets is well known to be approximately independent of the tube-to-pellet diameter ratio N, with a wide range of experimental data and correlations collapsing onto a similar trend, as reviewed by von Seckendorf and Hinrichsen [11]. For beds of solid cylindrical pellets, experimental measurements from Roshani [38] show an increase in the voidage for distances $< 0.5\ d_o$ from the wall as N decreased from ~22 to ~3. This is in good agreement with the voidage profiles reported here. The difference observed in the near-wall hydrodynamics, whereby the $N = 4.8$ bed shows a larger average axial velocity near the wall compared to the smaller beds, is in contradiction with the work of Moghaddam et al. [39] whose CFD simulations show the average axial velocity in the vicinity of the tube wall decreasing with N for hollow cylindrical pellets (albeit with a larger pellet hole than the pellets studied here). Whilst the discrepancy between the present results and those of Moghaddam et al. [39] could be due to the difference in pellet shape, it may also indicate the need to further develop particle resolved CFD simulations for more accurate representation of the near-wall hydrodynamics in narrow beds. Note that other CFD studies conducted for spherical pellets over a range of Reynolds numbers show an increase in the near-wall velocity with increasing tube-to-pellet diameter ratio from $N \approx 4$ to $N \approx 9$ [40, 41]. The higher average axial velocity near the wall in the larger ($N = 4.8$) bed is explainable considering the relative volume of the wall section and core/inner section in each bed. Because of the higher voidage close to the tube wall, the resistance to flow is lower and the velocity subsequently higher at the wall compared to the average in the core/inner section of the bed. As N increases, the core/inner section becomes a larger fraction of the total bed volume, and thus becomes a larger contribution to the bed-average velocity. Therefore, for the $N = 4.8$ bed, since the core section of the bed is larger compared to the smaller beds, the relative average velocity at the wall is larger. The larger amount of high-speed fluid at the wall in the $N = 4.8$ bed, as shown in Fig. 9, is further supported by the results shown in Table 3 and Fig. 6 which show an increase in the high-speed fluid fraction in the bed for $N = 4.8$ and show that this high-speed fluid is located predominantly at the tube wall. These findings have important implications for the wall-to-bed heat transfer in narrow packed beds and may help to give mechanistic insight into the complex relationship between transport properties and N observed in the literature [13]. Finally, the location of the maximum in the average axial velocity in the $N = 3.7$ bed at $\sim 1.3\ d_o$ helps to confirm the flow 'lane' effect seen in Fig. 3b. This is likely due to the bed structure at this particular N being especially ordered, as almost all pellets are adjacent to the

wall. Tang et al. [21] also observed from 2D MR velocity imaging measurements that in a bed of spherical pellets with $N = 2.7$, the maximum axial velocity was located near the centre of the bed rather than at the tube wall due to a large void near the centre of the bed. Whilst imaging a longer section of the bed may be needed to assess if this is a global, or simply a local, effect in this bed, this observation directly demonstrates that the local bed structure leads to changes in the flow pattern within the bed at particular values of N. As recently explained by Dixon, [13] changes in local bed structure, and thus local flow patterns, explain the strong dependence of heat transport properties on the particular value of N characterising a narrow packed bed.

3.3 Pellet Scale Hydrodynamics

To investigate the structure of the time-averaged velocity field at the pellet scale, the average velocity magnitude is shown as a function of distance from the nearest solid interface (either tube or wall) in Fig. 10. These plots do not represent the true velocity profile within an individual void within the bed. Rather, they should be interpreted as the average velocity as a function of distance from solid, which can give some insight to the spatial structure of the flow field at the pellet scale. Approximately 85% of the fluid in the bed is located at a distance $l < 0.15\, d_o$ from a solid interface, thus it is this region of the profiles that has the most influence on the overall hydrodynamics in the bed. All beds show a flow profile consistent with channel/duct flow, whereby the average velocity magnitude increases with increasing distance from solid interfaces. For distances $l < 0.15\, d_o$ the profiles for each bed are very similar and within error. The results shown in Fig. 10 demonstrate that the average flow characteristics at the pellet scale are independent of the tube-to-pellet diameter ratio, N.

To further investigate the hydrodynamics at the pellet scale, the flow in the pellet holes was investigated by segmenting the pellet holes from the rest of the bed

Fig. 10 Time-averaged normalized velocity magnitude, $|\overline{\mathbf{u}}|/U_{int}$, averaged across the bed as a function of perpendicular distance from the nearest solid boundary, l/d_o, for each bed studied. Error bars represent the uncertainty of the average value at each position
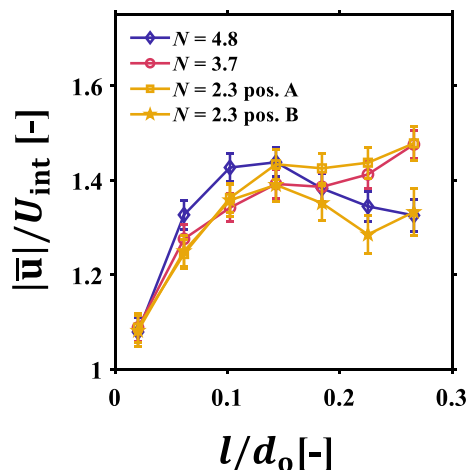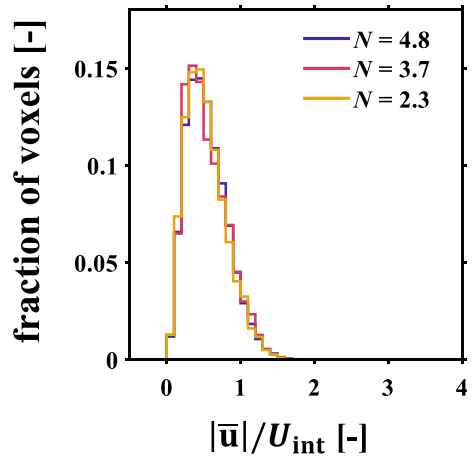
Fig. 11 Histogram of fluid speed, $|\overline{\mathbf{u}}|$, normalized by the interstitial velocity, U_{int}, for fluid within the pellet holes

and analysing the velocity of voxels located within these holes. Figure 11 shows the velocity histogram for fluid within the pellet holes. Comparing the histograms in Fig. 11 with the velocity magnitude histogram for the entire bed, shown in Fig. 5c, it is seen that the fluid within the pellet holes is much slower, on average, than the average fluid in the bed. This is likely due to the small diameter of the pellet holes ($d_{hole} = 1.3$ mm) which presents a significant resistance to flow. Further, Fig. 11 shows that the velocity magnitude distribution for fluid within pellet holes does not change with N. Thus, the flow characteristics within the pellet holes appear to be independent of the tube-to-pellet diameter ratio, for the pellets studied here. Taken together, the data shown in Figs. 10 and 11 show that the pellet scale hydrodynamics are independent of the tube-to-pellet diameter ratio, N, for the hollow cylinders studied in this work.

4 Conclusions

In this work, compressed sensing MR velocity imaging has been employed to investigate the effect of the tube-to-pellet diameter ratio, N, on the hydrodynamics at the bed and pellet scale for turbulent flows through beds of hollow cylindrical catalyst support pellets. MR velocity imaging was utilized to acquire 3D images of the time-average velocity in three different beds with $N = 4.8$, 3.7, and 2.3.

The 3D flow imaging results reveal some changes in the hydrodynamics with changing N. Whilst the bed-scale velocity distributions (axial, transverse, and velocity magnitude) are largely similar as a function of N, the high-velocity tail of the axial velocity and velocity magnitude distributions are larger for $N = 4.8$ compared to the smaller N beds. The fraction of high-speed fluid in the bed, quantified as $|\overline{\mathbf{u}}|/U_{int} > 2.5$, was indeed larger in the $N = 4.8$ bed compared to the smaller beds. Analysis of the 3D velocity images revealed that the increased amount of high-speed

fluid in the $N = 4.8$ bed was due to differences in the near-wall hydrodynamics with the $N = 4.8$ bed showing more high-speed fluid at the wall, and thus a larger average axial velocity at the wall, compared to the smaller N beds. Further, possibly due to the particular structuring in the bed at $N = 3.7$, extended flow lanes with high axial velocity were observed at a distance $\sim 1.3\ d_o$ from the tube wall. These flow lanes resulted in the maximum in the radial profile of axial velocity occurring not near the wall, but rather $\sim 1.3\ d_o$ from the tube wall. At the pellet-scale, the hydrodynamics were found to be independent of N, with the average velocity magnitude as a function of distance from solid interface showing a similar trend in all beds studied. The flow in pellet holes was also found to be independent of N for the pellets tested.

Taken together, the observed changes in the velocity field with N, namely the increase in high-speed fluid at the wall for $N = 4.8$ and the flow lanes at $N = 3.7$ give insight into how the hydrodynamics can change with particular values of N. These changes in hydrodynamics demonstrate the direct linkage between bed structure and hydrodynamics in narrow packed beds. This work demonstrates the capability of MR velocity imaging for obtaining full field measurements of the flow in packed beds using commercially relevant pellets and flow conditions. The observations reported here, and the insights gained, may help in understanding, and ultimately predicting, how transport properties change with N in narrow packed beds.

Declarations

Conflict of interest The authors have no relevant financial or non-financial interests to disclose.

Ethical approval Not applicable.

directly from the copyright holder. To view a copy of this licence, visit http://creativecommons.org/licenses/by/4.0/.

References

1. G. Jacobs, B. H. Davis, in *Multiph. Catal. React.* (Wiley, Hoboken, 2016), pp. 269–294.
2. I. Iliuta, F. Larachi, in *Multiph. Catal. React.* (Wiley, Hoboken, 2016), pp. 95–131.
3. S. Moran, K.-D. Henkel, in *Ullmann's Encycl. Ind. Chem.* (Wiley, Weinheim, 2016), pp. 1–49.
4. R.F. Benenati, C.B. Brosilow, AIChE J. **8**, 359 (1962)
5. J.S. Goodling, R.I. Vachon, W.S. Stelpflug, S.J. Ying, M.S. Khader, Powder Technol. **35**, 23 (1983)
6. A. De Klerk, AIChE J. **49**, 2022 (2003)
7. A.G. Dixon, J.H. Van Dongeren, Chem. Eng. Process. Process Intensif. **37**, 23 (1998)
8. A.G. Dixon, Ind. Eng. Chem. Res. **36**, 3053 (1997)
9. A.G. Dixon, Chem. Eng. Sci. **231**, 116305 (2021)
10. A.G. Dixon, B. Partopour, Annu. Rev. Chem. Biomol. Eng. **11**, 109 (2020)
11. J. von Seckendorff, O. Hinrichsen, Can. J. Chem. Eng. **99**, S703 (2021)
12. Z. Guo, Z. Sun, N. Zhang, M. Ding, X. Cao, Powder Technol. **319**, 445 (2017)
13. A.G. Dixon, Ind. Eng. Chem. Res. **60**, 9777 (2021)
14. D. Vortmeyer, R.P. Winter, Chem. Eng. Sci. **39**, 1430 (1984)
15. N. Jurtz, G.D. Wehinger, U. Srivastava, T. Henkel, M. Kraume, AIChE J. **66**, e16967 (2020)
16. R. Caulkin, X. Jia, C. Xu, M. Fairweather, R.A. Williams, H. Stitt, M. Nijemeisland, S. Aferka, M. Crine, A. Léonard, D. Toye, P. Marchot, Ind. Eng. Chem. Res. **48**, 202 (2009)
17. O. Bey, G. Eigenberger, Chem. Eng. Sci. **52**, 1365 (1997)
18. O. Bey, G. Eigenberger, Int. J. Therm. Sci. **40**, 152 (2001)
19. X. Ren, S. Stapf, B. Blümich, Chem. Eng. Technol. **28**, 219 (2005)
20. X. Ren, S. Stapf, B. Blümich, AIChE J. **51**, 392 (2005)
21. D. Tang, A. Jess, X. Ren, B. Bluemich, S. Stapf, Chem. Eng. Technol. **27**, 866 (2004)
22. J.D. Cooper, L. Liu, N.P. Ramskill, T.C. Watling, A.P.E. York, E.H. Stitt, A.J. Sederman, L.F. Gladden, Chem. Eng. Sci. **209**, 115179 (2019)
23. J.D. Cooper, A.P.E. York, A.J. Sederman, L.F. Gladden, Chem. Eng. J. **377**, 119690 (2019)
24. S. V. Elgersma, A. J. Sederman, M. D. Mantle, C. M. Guédon, G. J. Wells, L. F. Gladden, Chem. Eng. J. 145445 (2023)
25. M.H. Sankey, D.J. Holland, A.J. Sederman, L.F. Gladden, J. Magn. Reson. **196**, 142 (2009)
26. N.P. Ramskill, A.P.E. York, A.J. Sederman, L.F. Gladden, Chem. Eng. Sci. **158**, 490 (2017)
27. C. Guder, W. Wagner, J. Phys. Chem. Ref. Data **38**, 33 (2009)
28. S.E. Quiñones-Cisneros, M.L. Huber, U.K. Deiters, J. Phys. Chem. Ref. Data **41**, 23102 (2012)
29. D. Xiao, B.J. Balcom, J. Magn. Reson. **231**, 126 (2013)
30. O.V. Petrov, G. Ersland, B.J. Balcom, J. Magn. Reson. **209**, 39 (2011)
31. P.T. Callaghan, *Translational Dynamics and Magnetic Resonance: Principles of Pulsed Gradient Spin Echo NMR* (Oxford University Press, Oxford, UK, 2011)
32. H. Gudbjartsson, S. Patz, Magn. Reson. Med. **34**, 910 (1995)
33. M. Lustig, D. Donoho, J.M. Pauly, Magn. Reson. Med. **58**, 1182 (2007)
34. K. Karlsons, D.W. De Kort, A.J. Sederman, M.D. Mantle, H. De Jong, M. Appel, L.F. Gladden, J. Microsc. **276**, 63 (2019)
35. M. Benning, L. Gladden, D. Holland, C.B. Schönlieb, T. Valkonen, J. Magn. Reson. **238**, 26 (2014)
36. P. Magnico, Chem. Eng. Sci. **58**, 5005 (2003)
37. M. Giese, K. Rottschäfer, D. Vortmeyer, AIChE J. **44**, 484 (1998)
38. S. Roshani, Elucidation of local and global structural properties of packed bed configurations. University of Leeds (1990)
39. E.M. Moghaddam, E.A. Foumeny, A.I. Stankiewicz, J.T. Padding, Chem. Eng. Sci. X **5**, 100057 (2020)
40. M. Zhang, H. Dong, Z. Geng, Chem. Eng. Res. Des. **132**, 149 (2018)
41. A.G. Dixon, N.J. Medeiros, Fluids **2**, 56 (2017)

Authors and Affiliations

Scott V. Elgersma[1] · Andrew J. Sederman[1] · Michael D. Mantle[1] · Constant M. Guédon[2] · Gary J. Wells[3] · Lynn F. Gladden[1]

✉ Andrew J. Sederman
ajs40@cam.ac.uk

[1] Magnetic Resonance Research Centre, Department of Chemical Engineering and Biotechnology, University of Cambridge, Philippa Fawcett Drive, Cambridge CB3 0AS, UK

[2] Shell Global Solutions International B.V., Grasweg 31, Amsterdam 1031 HW, The Netherlands

[3] Shell Catalysts and Technologies US LP, 3333 Highway 6 South, Houston, TX 77082, USA